Nonaqueous synthesis of CoO$_x$/TiO$_2$ nanocomposites showing high photocatalytic activity of hydrogen generation

Yu-Fen Wang [a,1], Meng-Chun Hsieh [a,1], Jyh-Fu Lee [b], Chia-Min Yang [a,c,*]

[a] Department of Chemistry, National Tsing Hua University, Hsinchu 30013, Taiwan
[b] National Synchrotron Radiation Research Center, Hsinchu 30076, Taiwan
[c] Frontier Research Center on Fundamental and Applied Sciences of Matters, National Tsing Hua University, Hsinchu 30013, Taiwan

ABSTRACT

This paper describes a nonaqueous sol–gel preparation of *p–n* diode-type CoO$_x$/TiO$_2$ nanocomposites for photocatalytic hydrogen generation. Characterization results suggested that the nanocomposites consisted of highly crystalline anatase nanoparticles and Co$_3$O$_4$-like species. They showed composition-dependent activity for hydrogen production under ultraviolet light irradiation with methanol as a sacrificial agent. The nanocomposite with the optimum composition exhibited superior photocatalytic activity and a hydrogen evolution rate of 2.17 mmol g^{-1} h^{-1}. In comparison, the hydrogen evolution rates for the reference photocatalysts Degussa P25 and sodium tantalite measured under the same conditions were 20 μmol g^{-1} and 410 μmol g^{-1}, respectively. The stability and the concentration-dependent hydrogen production with methanol or ethanol as sacrificial agent were also studied. In addition, the nanocomposite was capable of producing hydrogen, albeit in small amount, in the sacrificial agent-free conditions in the phosphate-buffered solutions. The results show not only the uniqueness of the nonaqueous synthesis for highly active CoO$_x$/TiO$_2$ heterojunction photocatalysts, but also the possibility to further improve the photocatalytic activity of CoO$_x$/TiO$_2$ through surface engineering.

© 2013 Elsevier B.V. All rights reserved.

1. Introduction

Growing environmental concerns related to fossil fuels use, along with the ever-increasing energy demand, have strongly stimulated the search for clean energy systems [1,2]. Hydrogen can play an important role in the systems as an energy carrier [3], but about 95% H$_2$ is still derived from fossil fuels and obtained by steam reforming or catalytic decomposition processes [4–7]. For small- and medium-scale H$_2$ production, the photoactivated methods, including photocatalytic water splitting [8–12] and photoreforming of suitable oxygenates [13–16], are amenable and strategic alternatives. These methods involve the utilization of semiconductor materials to absorb light and generate electrons and holes for reduction and oxidation reactions, respectively [8–12]. The most extensively studied material is titanium dioxide (TiO$_2$), a low-cost, highly stable and *n*-type semiconductor [17,18]. TiO$_2$ and other semiconductive photocatalysts need to have high crystallinity to prevent electron–hole recombination in the bulk and thereby exhibit high photocatalytic activity [8–12,17,18]. Another important factor is crystalline phase, and anatase TiO$_2$ usually demonstrates higher activity than rutile because of a greater extent of recombination of charge carriers in rutile [17,18].

In addition, the recombination of photogenerated electrons and holes in TiO$_2$ can be greatly suppressed by forming heterojunctions with metals or semiconducting materials [8–12,17–19]. For the metal-TiO$_2$ heterojunctions, for example Pt/TiO$_2$ [8–12,19], the photogenerated electrons are trapped at Pt to reduce water and generate H$_2$. Alternatively, when a *p*-type semiconductor having proper band structure is deposited onto TiO$_2$, the inner electric field at the heterojunction may induce spatial separation of the photogenerated charge carriers, with the suppression of energy-wasteful recombination, and thereby improve the photocatalytic activity [11,20–22]. The *p–n* diode-type photocatalysts have attracted much attention in recent years [7,11,23–39], and TiO$_2$-based composites with *p*-type metal oxides (including NiO [27–31], Cu$_2$O [32], CuAlO$_2$ [33], CoO [34,35], Bi$_2$O$_3$ [32], ZnMn$_2$O$_4$ [32] and nitrogen-doped ZnO [36]), selenium [37], AgGaS$_2$ [38] and boron-doped diamond [38] have been prepared and studied. Although these composites generally perform excellently for photodegradation of organic pollutants, their activities for photocatalytic H$_2$ generation have not been well studied and evaluated yet.

We herein report a direct synthesis of nanocomposites of TiO$_2$ and cobalt oxide for photocatalytic H$_2$ production. Cobalt oxides

* Corresponding author at: Department of Chemistry, National Tsing Hua University, Hsinchu 30013, Taiwan. Tel.: +886 3 5731282; fax: +886 3 5165521.
E-mail address: cmyang@mx.nthu.edu.tw (C.-M. Yang).
[1] Both these authors contributed equally to this work.

(CoO_x), such as CoO, Co_2O_3 and Co_3O_4, are p-type semiconductors with interesting electronic and magnetic properties that may be attractive and suitable to form diode-type photocatalysts with TiO_2. However, much attention has been focused on NiO/TiO_2 photocatalysts [27–31] that exhibited greater enhancement in photocatalytic activity than reported CoO_x/TiO_2 [34,35]. In this study, we successfully prepared highly active CoO_x/TiO_2 photocatalysts by a nonaqueous sol–gel process [40–46]. The CoO_x/TiO_2 nanocomposites consisted of highly crystalline anatase nanoparticles with Co_3O_4-like species attached on the surface. With an optimum composition, the nanocomposite exhibited superior and stable photocatalytic activity for H_2 generation with methanol or ethanol as sacrificial agent. Furthermore, we found that H_2 could be produced, albeit in small amounts, under sacrificial agent-free conditions in the phosphate-buffered solution. Techniques including X-ray photoelectron spectroscopy (XPS), electron paramagnetic resonance (EPR) spectroscopy and X-ray absorption spectroscopy (XAS) were used to extensively characterize the CoO_x/TiO_2 nanocomposites, especially the oxidation state and coordination environment of CoO_x species.

2. Experimental

2.1. Catalyst preparation

In a typical synthesis of CoO_x/TiO_2 nanocomposite, titanium tetrachloride ($TiCl_4$, 1.0 M dichloromethane solution, 9.2 mL) and cobalt (III) acetylacetonate ($Co(acac)_3$) were added to benzyl alcohol (BA) (dried over Molecular Sieve 4A and stored in a glove box) under vigorous stirring in an inert atmosphere at room temperature. The molar composition was 1 $TiCl_4$:x $Co(acac)_3$:20 BA, where x = 0, 0.05, 0.1, 0.2, 0.3, 0.4 and 0.5. The mixture was subjected to microwave heating ($10\,°C\,min^{-1}$ heating ramp) at $120\,°C$ for 2 h using a CEM MARS microwave digestion system operating at a frequency of 2.45 GHz. The resulting suspension was centrifuged at 6000 rpm for 20 min, and the precipitate was washed with BA and then acetone. The solvents were removed by centrifugation after each washing step. The as-synthesized product was collected and dried in air at $60\,°C$ and was subsequently heated at $400\,°C$ for 3 h. The samples are designated as CoTi-x, where x denotes the mole percentage of Co and Ti (Co/Ti × 100%) in the samples determined by inductively coupled plasma-mass spectroscopy (ICP-MS).

2.2. Catalyst characterization

ICP-MS data were obtained using a Perkin-Elmer SCIEX-ELAN 5000 device. X-ray diffraction (XRD) patterns were measured on a Bruker D8 diffractometer using Cu Kα radiation as X-ray source. Transmission electron microscopic (TEM) images were recorded on a JEOL JEM-2100 electron microscope operating at 200 kV equipped with an energy dispersion spectrometer (EDS). UV–visible absorption spectra were recorded on a JASCO V-650 spectrophotometer equipped with a diffuse reflection accessory. XPS spectra were collected on a Kratos Axis Ultra spectrometer with Mg Kα X-ray source. EPR spectra were obtained at 77 K with a Bruker Elexsys E-580 spectrometer operating in the X-band with a microwave power of 15 mW and a resonance frequency of ca. 9.63 GHz using 100 kHz modulation. The g values of the signals were measured relative to DPPH (g = 2.0036). Co K-edge XAS spectra were measured on the beamline 17 C at the National Synchrotron Radiation Research Center (NSRRC, Taiwan) with storage ring energy of 1.5 GeV. In a typical XAS experiment, about 100 mg of sample was pressed to form self-supporting wafers before being mounted in a cell. Measurements were taken at room temperature in step scanning mode, and multiple scans were obtained to improve the signal-to-noise ratio. X-ray

signal was detected in transmission mode for most of the sample except CoTi-2.9, for which fluorescence mode was applied.

2.3. Photocatalytic hydrogen generation

The experiments were carried out in a closed quartz reaction cell. A photocatalyst (0.1 g) was dispersed in aqueous solution of methanol or ethanol (100 mL, 10–50 vol%). The suspension was magnetically stirred and continuously purged with an argon flow for at least 30 min before irradiation in order to remove dissolved air. The suspension was then irradiated with ultraviolet (UV) light using a 500 W Hg–Xe arc lamp (Oriel) equipped with a short-wave pass filter (Newport, cut-off wavelength of 400 nm). The power density of the irradiation on reaction cell was measured $33\,mW\,cm^{-2}$. The evolved gases were analyzed by a gas chromatograph (GC, Shimadzu; GC-2014) using a molecular sieve 5A column and equipped with a thermal conductivity detector and argon as carrier gas. The average rate of H_2 evolution was determined by averaging the total amount of H_2 generated within 2 h. Additionally, the best catalyst Co-Ti-2.9 (0.1 g) was dispersed in alcohol-free phosphate buffered solutions (PBSs, 100 mL, 0.1 M) and was irradiated by UV. PBSs with a pH of 6.0, 7.0 and 8.0 were prepared by dissolving calculated amounts of sodium phosphate (NaH_2PO_4) in deionized water followed by pH adjustment with sodium hydroxide.

3. Results and discussion

The samples synthesized via the nonaqueous sol–gel route were in excellent yields (>95%) based on the titanium content. For CoO_x/TiO_2 nanocomposites, the Co/Ti ratios (determined by ICP-MS) are significantly lower (about 18–30%) than the molar ratios of $Co(acac)_3$ and $TiCl_4$ in the synthesis mixtures. This may be associated to slower nonhydrolyic condensation of CoO_x in nonaqueous synthesis systems [42,43]. Fig. 1 shows the XRD patterns of the samples. The cobalt-free sample (CoTi-0) exhibited broad reflections that could be assigned to the anatase phase without any indication of other crystalline polymorphs as byproducts. By applying the Scherrer equation on the (1 0 1) reflection [44–46], the crystalline size of anatase in CoTi-0 was estimated to be 14.4 nm. A comparison with the size for the as-synthesized sample (around 6.5 nm, cf. Fig. S1 in the Supplementary Material) revealed severe sintering of anatase nanocrystals during the heating at $400\,°C$. On the other hand, the addition of $Co(acac)_3$ not only retarded the anatase growth during the nonaqueous synthesis to result in smaller nanocrystals in the as-synthesize nanocomposites but also suppressed thermal sintering of the nanocrystals. The estimated crystalline sizes of anatase in CoTi-2.9, CoTi-5.2 and CoTi-14.3 were 9.6 nm, 7.6 nm and 6.5 nm, respectively. It was noted that no reflections attributed to crystalline cobalt-containing species were observed for CoO_x/TiO_2 nanocomposites with a Co/Ti ratio lower than 3.9%. On the other hand, relatively sharp reflections in the XRD patterns of CoTi-7.8 and CoTi-14.3 (cf. Fig. 1) indicated the presence of the spinel Co_3O_4 particles (JCPDS file 80-1545) in these samples. The Co_3O_4 particles were formed during heat treatment at $400\,°C$ from hydroxide species in the as-synthesized samples (cf. Fig. S1 in the Supplementary Material).

Consistent with XRD analysis, TEM showed that the anatase particles in CoTi-0 are around 15–20 nm in size (cf. Fig. S2 in the Supplementary Material), and those in CoTi-2.9 and CoTi-5.2 are smaller (cf. inset in Fig. 2). As shown in Fig. 2, the particles in all the samples are single-crystalline, and the lattice fringes corresponding to the {1 0 1} planes (d-spacing of 0.35 nm) can be clearly observed throughout each particle [44–46]. The Co/Ti ratios for the nanocomposites analyzed by EDS were very close to the values determined
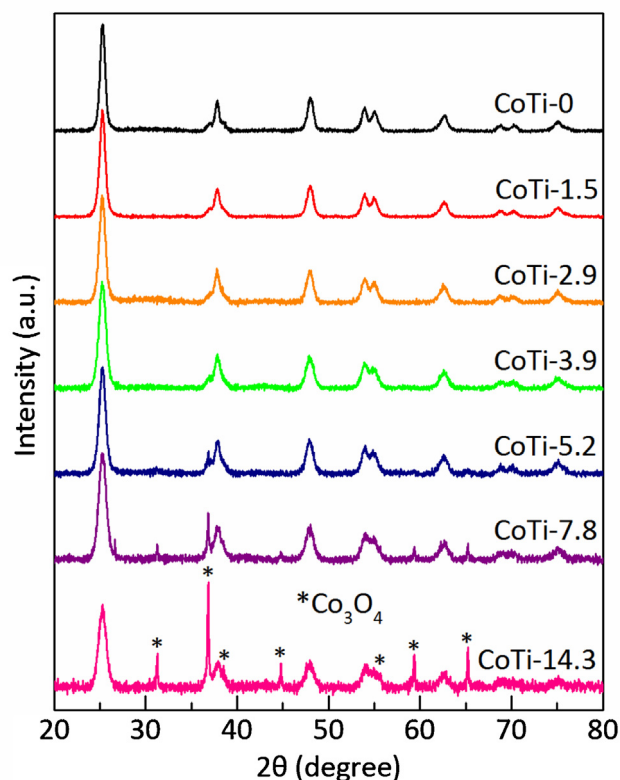
Fig. 1. XRD patterns of CoO_x/TiO_2 nanocomposites.

Fig. 2. TEM images of (a) CoTi-2.9 and (b) CoTi-5.2.

by ICP-MS. Discrete CoO_x particles were not observed in CoTi-2.9, whereas only a few tiny domains with lattice fringes (d-spacing of 0.245 nm) that may be assigned to the {3 1 1} planes of the spinel Co_3O_4 [9,24] could be discerned in the TEM images of CoTi-5.2 (cf. Fig. 2b).

The photocatalytic activities of CoO_x/TiO_2 for H_2 production were examined with methanol as a sacrificial agent. Fig. 3a shows the average rates of H_2 evolution for CoO_x/TiO_2 in the aqueous solution of methanol (10 vol%) under UV irradiation. All the cobalt-containing nanocomposites except CoTi-14.3 were more active than the pure-anatase CoTi-0, and the best catalyst was CoTi-2.9 that exhibited very high H_2 evolution rate of 2.17 mmol g^{-1} h^{-1}. All the CoO_x/TiO_2-catalyzed reactions produced carbon dioxide (CO_2) as the only product from methanol photooxidation as revealed by GC. Interestingly, the photocatalytic activity was very sensitive to the Co loading and a volcano-shape relationship between H_2 evolution rate and Co/Ti ratio was observed. Since the crystallinity and size of anatase nanocrystals in the samples did not differ much and would have limited influence on the activity, the relationship should be associated with the amount, distribution and chemical state of cobalt in CoO_x/TiO_2. Obviously, CoO_x needs to be attached to anatase nanocrystals in order to form p–n heterojunction to effectively separate the charge carriers generated upon irradiation. Increasing the loading of CoO_x may result in more heterojunctions in the nanocomposite, but too much loading would largely reduce the exposed surface of anatase nanocrystals and thereby decrease the chance for the photogenerated electrons to reduce water and produce H_2.

For comparison, the most frequently applied benchmark photocatalysts including Degussa P25 (~25 nm in size and composed of about 80% anatase and 20% rutile) and sodium tantalite ($NaTaO_3$, prepared according to the reported procedure reported by Kato et al. [47]) were also tested under the same reaction conditions. The rate of H_2 evolution for P25 was only about 20 μmol g^{-1} h^{-1},

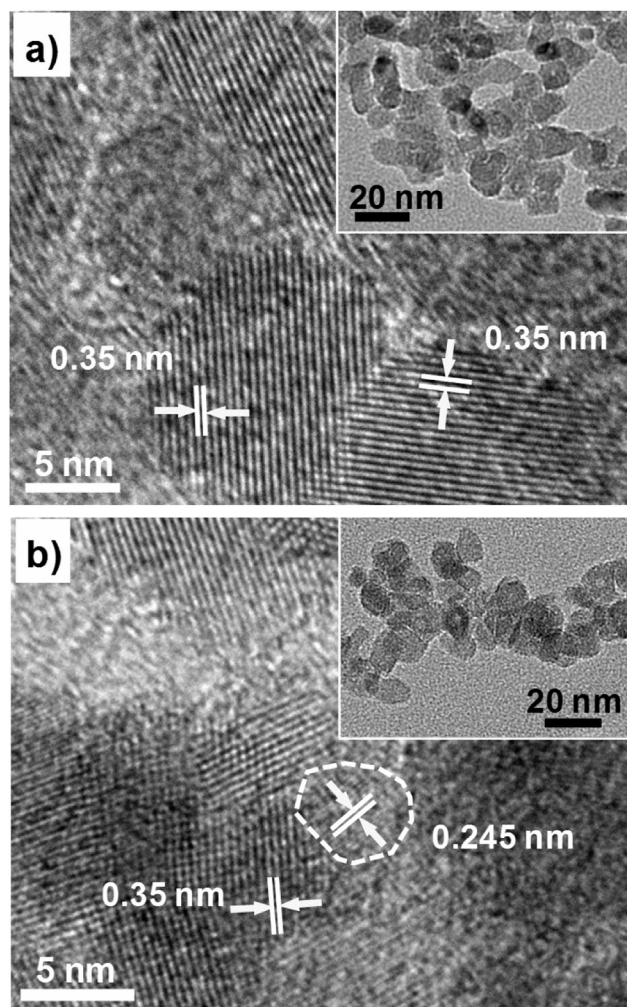one fifth of the rate of pure-anatase CoTi-0 (cf. Fig. 3b). This may be attributed to the smaller particle size and higher anatase crystallinity of CoTi-0 as compared to P25. $NaTaO_3$ was more active, with a H_2 evolution rate of 410 μmol g^{-1} h^{-1}, but the activity was still much lower than that of CoTi-2.9. We found that, by using the two photocatalysts as reference samples, the photocatalytic activity of CoTi-2.9 is comparable to the most active TiO_2-based Pt-containing photocatalysts [11]. Unfortunately, CoTi-2.9 and other CoO_x/TiO_2 were only UV-active and exhibited no activity with visible light irradiation despite that the nanocomposites were colored with CoO_x (Fig. S3 in the Supplementary Material). We also prepared a reference CoO_x/TiO_2 by simple impregnation of anatase nanocrystals (i.e. CoTi-0) with $Co(acac)_3$ followed by the same heat treatment to result in a sample with Co/Ti ratio of 2.9%. The rate of H_2 evolution for the sample (designated as CoTi-2.9im in Fig. 3b) was 1.24 mmol g^{-1} h^{-1}. Another reference sample prepared by using cobalt nitrate instead of $Co(acac)_3$ also exhibited similar H_2 evolution rate. The results indicated that the nonaqueous synthesis is a unique method to prepare highly active CoO_x/TiO_2 and probably also other oxide-based p–n heterojunction photocatalysts.

Fig. 4a shows the time courses of H_2 evolution from 10 vol% aqueous methanol solution in the presence of CoTi-2.9 under UV irradiation. The reactions were conducted for 24 h with three intermediate stops to separate the photocatalyst by centrifugation and re-disperse it in a fresh methanol solution after every 6 h of irradiation. The activity was only decreased very slightly during consecutive cycles, suggesting that CoTi-2.9 is a rather
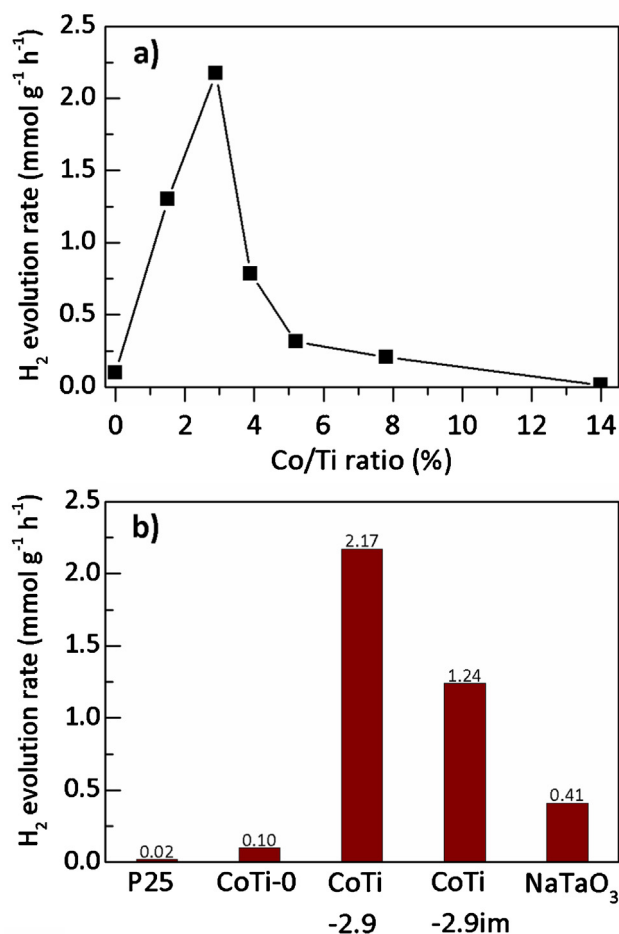
Fig. 5. H_2 evolution rates for CoTi-2.9 (0.1 g) in aqueous solutions (100 mL) of methanol or ethanol under UV irradiation.

Fig. 3. (a) H_2 evolution rates for CoO_x/TiO_2 (0.1 g) in 10 vol% aqueous methanol solution (100 mL) under UV irradiation. (b) Comparison of H_2 evolution rates for selected samples.
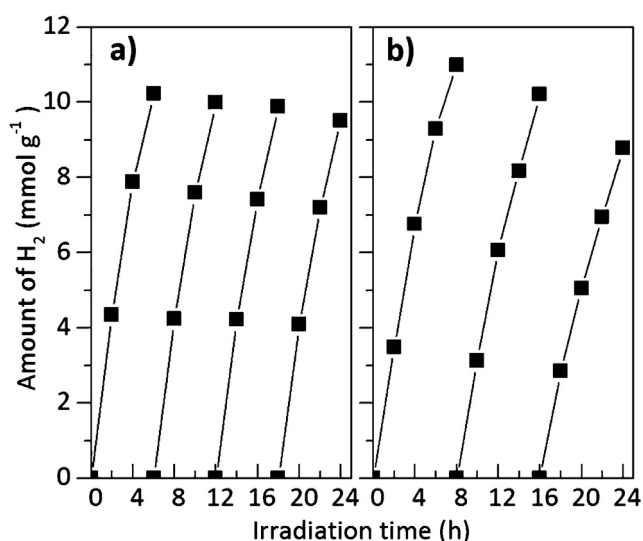

Fig. 4. Overall H_2 production in 10 vol% aqueous methanol solution (100 mL) under UV irradiation by CoTi-2.9 (0.1 g).
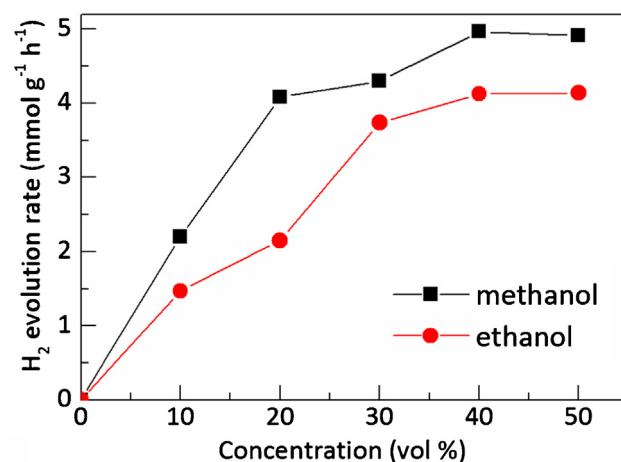
stable UV-active photocatalyst for H_2 production. After the 24-h UV irradiation, the same photocatalyst was again dispersed in 10 vol% methanol solution and the photocatalytic reactions were further conducted for another 24 h with two intermediate stops to flow argon through the reaction cell to remove gaseous species after every 8 h of irradiation without changing the reaction solution. It was found that the amount of photogenerated H_2 decreased during the second and third cycles (cf. Fig. 4b). The factor of methanol consumption alone could not be responsible for the decreased H_2 production. We speculated that it might be also attributed to the accumulation of dissolved CO_2 that might cause a slight decrease in solution pH and affect the surface properties of both CO_x and TiO_2 [17].

We further examined the effects of the concentration of methanol on the rate of H_2 evolution catalyzed by CoTi-2.9, and additionally ethanol was applied as a sacrificial agent. The results are shown in Fig. 5. The H_2 evolution rate increased as increasing the concentration of methanol or ethanol until it approached around 40 vol% at which the rates seemed to reach maximum values of 4.96 mmol g^{-1} h^{-1} and 4.12 mmol g^{-1} h^{-1} for methanol and ethanol, respectively. The lower H_2 production rate for ethanol may be attributed to the presence of carbon–carbon bond in the molecule that is relatively difficult to be cleaved photocatalytically. We found that acetaldehyde was the main byproducts of ethanol photooxidation detected in the gas stream, with ethylene, CO_2 and methane as minor byproducts. The results might also suggest that the CoO_x/TiO_2 nanocomposite mainly catalyzed the dehydrogenation of ethanol to produce H_2 under UV irradiation.

The CoO_x/TiO_2 nanocomposites were further characterized by various techniques to obtain more information about the nanocomposites, especially the oxidation states and coordination environment of the CoO_x. Fig. 6 shows the XPS and EPR spectra of CoTi-2.9, CoTi-5.2 and CoTi-14.3. The binding energies of 458.8 eV for Ti $2p_{3/2}$ and 464.5 eV for Ti $2p_{1/2}$ were observed, which are typical of that for TiO_2. The Co 2p spectra contain $2p_{3/2}$ and $2p_{1/2}$ peaks at around 780.7 eV and 796.7 eV, respectively, that are very close to those of the spinel Co_3O_4 [24,48]. The relatively sharp peaks and very weak satellite structure in the spectrum of CoTi-14.3 are characteristics of the spinel Co_3O_4 with low-spin octahedrally coordinated Co^{3+} and tetrahedrally coordinated Co^{2+} [48]. For CoTi-2.9 and Co-Ti-5.2, however, the position of the weak peaks could not be precisely determined and the possibility of CoO_x being CoO-like species could not be ruled out. On the other hand, all the samples showed a signal at $g = 2.00$ in the EPR spectra that may be assigned to paramagnetic adduct of oxygen and Co^{2+} on oxide surface [49,50].
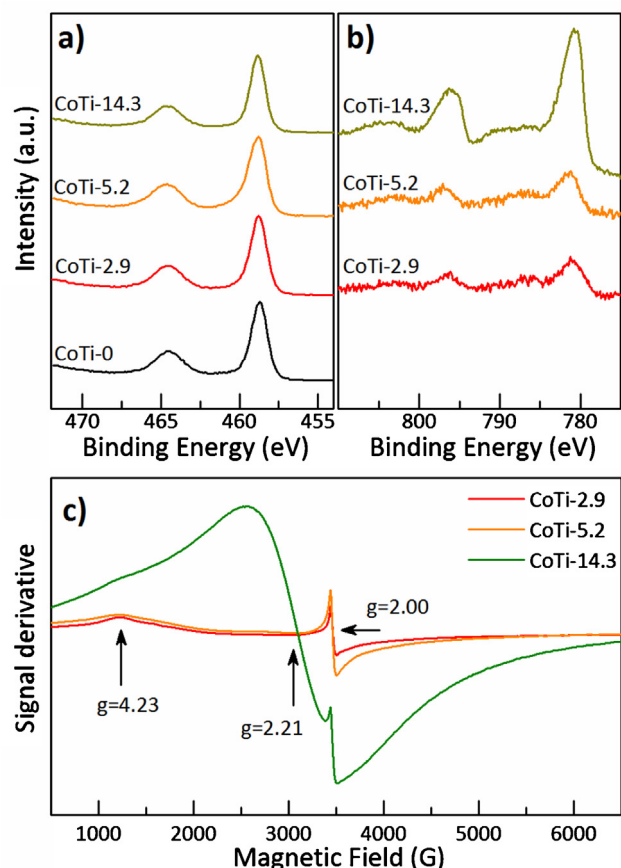
Fig. 6. (a) Ti 2p and (b) Co 2p XPS spectra and (c) EPR spectra of selected samples. (For interpretation of the references to spectra in figure legend, the reader is referred to the web version of the article.)

The adduct was considered to be in the form of $[O_2 \cdot Co^{2+}]$ instead of $[(O_2^-) \cdot Co^{3+}]$ because no hyperfine splitting was observed [49]. For CoTi-14.3, the signal at $g = 2.21$ again suggested the presence of Co_3O_4 in the sample [51]. Additionally, a very weak signal at $g = 4.23$, previously being assigned to the high-spin Co^{2+} ions occupying either octahedral or distorted tetrahedral sites [49,50], was also observed for the three samples. Therefore, based on the results of XPS and EPR, we could conclude that the CoTi-x samples had Co^{2+} on the surface of CoO_x and that CoTi-14.3 was mainly composed of TiO_2 and Co_3O_4 whereas the CoO_x species in CoTi-2.9 and CoTi-5.2 could be either CoO or Co_3O_4.

The coordination environment of cobalt was further studied by XAS. Fig. 7a shows the normalized X-ray absorption near-edge structure (XANES) spectra at Co K-edge for the three samples and reference samples including CoO, Co_3O_4 and $LiCoO_2$. All the samples with Co^{2+} and/or Co^{3+} showed absorption edge at around 7720 eV. For the three samples, the spectra resemble the profile of Co_3O_4 more than that of CoO. The resemblance becomes more pronounced when comparing the first derivatives of the spectra and the k^3-weighted extended X-ray absorption fine structure (EXAFS) spectra (Fig. S4 in the Supplementary Material). The Fourier transforms of the k^3-weighted EXAFS data are shown in Fig. 7b, and the results of the refinements for the first three coordination shells (two for references CoO and $LiCoO_2$) are summarized in Table 1. In agreement with the results of XPS and EPR, CoTi-5.2 and CoTi-14.3 presented interatomic distances (Rs) that are very close to those found in reference Co_3O_4, with the first Co–O shell at ~1.92 Å and the second and third Co–Co shells at ~2.85 Å and ~3.36 Å, respectively [52]. The low Co–O and Co–Co coordination numbers (CNs)
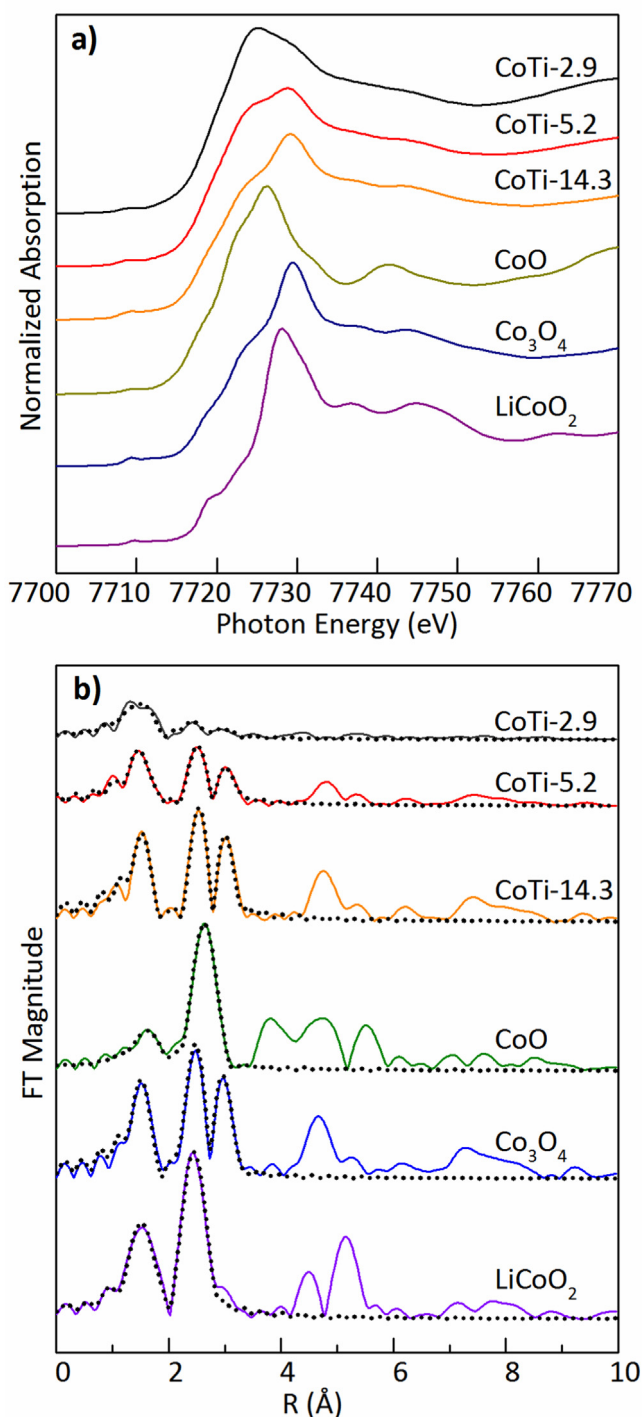

Fig. 7. (a) Normalized Co K-edge XANES spectra and (b) Fourier transforms of Co K-edge k^3-weighted EXAFS data (solid lines) and fitted results (dashed lines) for selected CoTi-x and reference samples. Note that the phase shifts were not corrected.

reflect the small size of Co_3O_4 in the nanocomposites. For CoTi-2.9, the Fourier transform also looks closer to the profile for Co_3O_4 than to that for CoO. In addition, the best fit of the data suggest the presence of a Co–Ti coordination shell for the sample with $R = 2.86$ Å and CN = 1.2 accompanying with varied distances of the fist Co–O shell ($R = 1.95$ Å, CN = 3.3) and the third Co–Co shell ($R = 3.27$ Å, CN = 0.9). Since the technique measures the average environment of the X-ray absorbing elements, the analysis suggests that the cobalt atoms in CoTi-2.9 mainly exist as Co_3O_4 – like clusters on anatase TiO_2.

Table 1
Curve-fitting results of the EXAFS data at Co K-edge[a].

Sample	Shell	CN	R (Å)	σ^2 (Å^2)	R factor (%)
CoTi-2.9	Co–O	3.3	1.95	0.0090	0.250
	Co–Ti	1.2	2.86	0.0013	
	Co–Co	0.9	3.27	0.0070	
CoTi-5.2	Co–O	2.9	1.91	0.0054	0.068
	Co–Co	1.8	2.89	0.0029	
	Co–Co	3.2	3.37	0.0048	
CoTi-14.3	Co–O	4.0	1.92	0.0051	0.042
	Co–Co	2.9	2.89	0.0029	
	Co–Co	5.6	3.36	0.0050	
CoO	Co–O	6.0	2.12	0.0078	0.004
	Co–Co	12.0	3.02	0.0074	
Co$_3$O$_4$	Co–O	5.3	1.92	0.0034	0.023
	Co–Co	4.0	2.85	0.0038	
	Co–Co	8.0	3.36	0.0060	
LiCoO$_2$	Co–O	5.7	1.92	0.0018	0.017
	Co–Co	5.6	2.82	0.0025	

[a] CN: coordination number; R: interatomic distance; σ^2: Debye-Waller factor.

Fig. 9. H$_2$ evolution rates for CoTi-2.9 (0.1 g) in pure water and PBSs (100 mL) at pH 6.0, 7.0 and 8.0 under UV irradiation for 2 h.

Based on the results obtained in this study and the information of the band structures of anatase TiO$_2$ and CoO$_x$ [11,53], we schematically represent the photocatalytic H$_2$ production in aqueous methanol solution by the UV-active CoTi-2.9 and other CoO$_x$/TiO$_2$ in Fig. 8. The band structures of CoO and Co$_3$O$_4$ are quite similar and, as reported by Zhang et al. [53] the top level of the valence band and the bottom level of the conduction band of Co$_3$O$_4$ nanoparticles are 2.52 V and 0.09 V, respectively, relative to the normal hydrogen electrode (NHE). When the heterojunction between n-type TiO$_2$ and p-type CoO$_x$ is formed, the Fermi level aligns and the band structures of two semiconductors shift correspondingly. Upon UV irradiation, the photoexcited electrons in the conduction band of TiO$_2$ reduce water to produce H$_2$ whereas the photogenerated holes are transferred to the valence band of CoO$_x$ for methanol oxidation to produce CO$_2$. The conduction band level of CoO$_x$ might be still slightly lower (i.e. more positive) than that of TiO$_2$ after forming the heterojunction so that the electrons photoexcited by visible light could not be effectively transferred to TiO$_2$ for H$_2$ evolution. On the other hand, although the valence band of CoO$_x$ is higher than that of TiO$_2$, it is much lower than the redox potential of O$_2$/H$_2$O (1.23 V vs. NHE). As a result, the nanocomposites should not be able to oxidize water and catalyze photochemical water splitting. Indeed, no H$_2$ was detected when CoTi-2.9 was
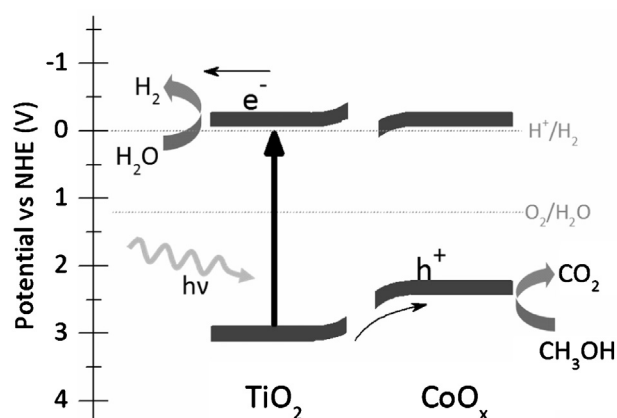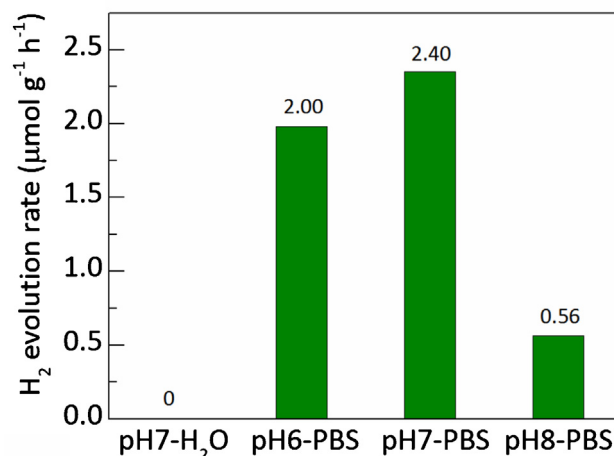
dispersed in pure water under UV irradiation (cf. Fig. 9). Knowing that the band levels of oxide materials usually shift with a change in solution pH ($\sim$−0.059 V pH^{-1}) [10,11], we also conducted the reaction in aqueous solutions of sodium hydroxide with pH up to 9.5 but still could not detect any H$_2$.

Finally, as inspired by the studies of Nocera and co-workers on a Co^{3+}-phosphate cluster that is capable of oxidizing water to produce O$_2$ photocatalytically at neutral pH [54,55], we prepared phosphate-buffered solutions (PBSs) at pH = 6.0, 7.0 and 8.0 and dispersed CoTi-2.9 in these solutions for photocatalytic studies. To our surprise, we observed H$_2$ generation in all the three PBSs and the highest H$_2$ evolution rate of 2.4 μmol g^{-1} h^{-1} was found in the PBS at pH 7.0 (cf. Fig. 9). Although the rate was low, the reaction could continue for hours without showing significant decrease in H$_2$ evolution rate. Unfortunately, O$_2$ could not be detected mainly due to its small amount of production and the detection limit of GC. Obviously, phosphate ions are crucial for the H$_2$ production photocatalyzed by CoTi-2.9. For the Co^{3+}-phosphate cluster reported by Nocera et al. [55] the mechanism of water splitting involves proton-coupled electron transfer and phosphate plays the essential role in facilitating rapid proton transfer with the concomitant oxidation of Co^{3+} to Co^{4+}. For CoTi-2.9, similar cluster may be formed when the surface Co^{2+} is oxidized by the photogenerated holes and similar chemistry of water splitting might also take place. While further studies are necessary to elucidate the mechanism of photocatalytic H$_2$ generation by CoTi-2.9 in PBSs, the results show the possibility to improve the photocatalytic activity of CoO$_x$/TiO$_2$ nanocomposites through surface engineering.

4. Conclusions

We have successfully applied a nonaqueous sol–gel process to prepare p–n diode-type CoO$_x$/TiO$_2$ nanocomposites consisting of anatase nanocrystals and Co$_3$O$_4$-like species. The nanocomposite with the optimum Co/Ti ratio exhibits superior and stable activity for photocatalytic hydrogen generation with methanol or ethanol as sacrificial agent under UV irradiation. The photooxidation of methanol produces carbon dioxide as the only product, whereas the dehydrogenation of ethanol takes place photocatalytically. The nanocomposite also shows the capability of producing hydrogen in the sacrificial agent-free conditions in the phosphate-buffered solutions. The results show not only the uniqueness of the nonaqueous synthesis for forming highly active CoO$_x$/TiO$_2$ heterojunction

Fig. 8. Schematic diagram of photocatalytic H$_2$ production in aqueous methanol solution under UV irradiation by CoO$_x$/TiO$_2$ involving hole transfer from n-type TiO$_2$ to p-type CoO$_x$.

photocatalysts, but also the possibility to further enhance the photocatalytic activity through surface engineering.

Acknowledgement

Appendix A. Supplementary data

Supplementary data associated with this article can be found, in the online version, at http://dx.doi.org/10.1016/j.apcatb.2013.05.073.

References

[1] C.D. Thomas, A. Cameron, R.E. Green, M. Bakkenes, L.J. Beaumont, Y.C. Collingham, B.F.N. Erasmus, M.F. de Siqueira, A. Grainger, L. Hannah, L. Hughes, B. Huntley, J.A.S. van, G.F. Midgley, L. Miles, M.A. Ortega-Huerta, P.A. Townsend, O.L. Phillips, S.E. Williams, Nature 427 (2004) 145–148.
[2] S. Zinoviev, F. Müller-Langer, P. Das, N. Bertero, P. Fornasiero, M. Kaltschmitt, G. Centi, S. Miertus, ChemSusChem 3 (2010) 1106–1133.
[3] A. Zuttel, A. Borgschulte, L. Schlapbach (Eds.), Hydrogen as a Future Energy Carrier, Wiley-VCH Verlag GmbH & Co, Weinheim. KGaA, 2008.
[4] R.D. Cortright, R.R. Davda, J.A. Dumesic, Nature 418 (2002) 964–967.
[5] S. Sato, S.-Y. Lin, Y. Suzuki, H. Hatano, Fuel 82 (2003) 561–567.
[6] Y. Fu, J. Shen, Journal of Catalysis 248 (2007) 101–110.
[7] R.M. Navarro, M.A. Pena, J.L.G. Fierro, Chemical Reviews 107 (2007) 3952–3991.
[8] M. Matsuoka, M. Kitano, M. Takeuchi, K. Tsujimaru, M. Anpo, J.M. Thomas, Catalysis Today 122 (2007) 51–61.
[9] R. van de Krol, Y. Liang, J. Schoonman, Journal of Materials Chemistry 18 (2008) 2311–2320.
[10] A. Kudo, Y. Miseki, Chemical Society Reviews 38 (2009) 253–278.
[11] X. Chen, S. Shen, L. Guo, S.S. Mao, Chemical Reviews 110 (2010) 6503–6570.
[12] D. Barreca, G. Carraro, V. Gombac, A. Gasparotto, C. Maccato, P. Fornasiero, E. Tondello, Advanced Functional Materials 21 (2011) 2611–2623.
[13] X. Fu, J. Long, X. Wang, D.Y.C. Leung, Z. Ding, L. Wu, Z. Zhang, Z. Li, X. Fu, International Journal of Hydrogen Energy 33 (2008) 6484–6491.
[14] R.M. Navarro, M.C. Sánchez-Sánchez, M.C. Alvarez-Galvan, F. del Valle, J.L.G. Fierro, Energy and Environmental Science 2 (2009) 35–54.
[15] V.M. Daskalaki, D.I. Kondarides, Catalysis Today 144 (2009) 75–80.
[16] C. Ampelli, G. Centi, R. Passalacqua, S. Perathoner, Energy and Environmental Science 3 (2010) 292–301.
[17] A.L. Linsebigler, G. Lu, J.T. Yates, Chemical Reviews 95 (1995) 735–758.
[18] X. Chen, S.S. Mao, Chemical Reviews 107 (2007) 2891–2959.
[19] A. Fujishima, K. Honda, Nature 238 (1972) 37–38.
[20] A.J. Nozik, Applied Physics Letters 30 (1977) 567–569.
[21] O. Khaselev, J.A. Turner, Science 280 (1998) 425–427.
[22] H.G. Kim, P.H. Borse, J.S. Jang, E.D. Jeong, O.S. Jung, Y.J. Suh, J.S. Lee, Chemical Communications (2009) 5889–5891.
[23] J.S. Jang, H.G. Kim, J.S. Lee, Catalysis Today 185 (2012) 270–277.
[24] M. Long, W. Cai, J. Cai, B. Zhou, X. Chai, Y. Wu, Journal of Physical Chemistry B 110 (2006) 20211–20216.
[25] C. Yang, W. Wang, Z. Shan, F. Huang, Journal of Solid State Chemistry 182 (2009) 807–812.
[26] S.Z. Kang, Y.K. Yang, W. Bu, J. Mu, Journal of Solid State Chemistry 182 (2009) 2972–2976.
[27] S. Chen, S. Zhang, W. Liu, W. Zhao, Journal of Hazardous Materials 155 (2008) 320–326.
[28] J. Yu, W. Wang, B. Cheng, Chemistry – An Asian Journal 5 (2010) 2499–2506.
[29] J. Lin, J. Shen, R. Wang, J. Cui, W. Zhou, P. Hu, D. Liu, H. Liu, J. Wang, R.I. Boughton, Y. Yue, Journal of Materials Chemistry 21 (2011) 5106–5113.
[30] Y. Ku, C.N. Lin, W.M. Hou, Journal of Molecular Catalysis A 349 (2011) 20–27.
[31] C.J. Chen, C.H. Liao, K.C. Hsu, Y.T. Wu, J.C.S. Wu, Catalysis Communications 12 (2011) 1307–1310.
[32] Y. Bessekhouad, D. Robert, J.V. Weber, Catalysis Today 101 (2005) 315–321.
[33] R. Brahimi, Y. Bessekhouad, A. Bouguelia, M. Trari, Journal of Photochemistry and Photobiology A 186 (2007) 242–247.
[34] M.H. Kim, Korean Journal of Chemical Engineering 22 (2005) 839–843.
[35] G. Zhang, H. Huang, W. Li, F. Yu, H. Wu, L. Zhou, Electrochimica Acta 81 (2012) 117–122.
[36] S. Chen, W. Zhao, W. Liu, S. Zhang, Applied Surface Science 255 (2008) 2478–2484.
[37] T.N.R. De, C.R. Chenthamarakshan, K. Rajeshwar, E.J. Tacconi, Journal of Physical Chemistry B 109 (2005) 11953–11960.
[38] J.S. Jang, S.J. Hong, J.Y. Kim, J.S. Lee, Chemical Physics Letters 475 (2009) 78–81.
[39] J. Yuan, H. Li, S. Gao, Y. Lin, H. Li, Chemical Communications 46 (2010) 3119–3121.
[40] A. Vioux, Chemistry of Materials 9 (1997) 2292–2299.
[41] M. Niederberger, M.H. Bartl, G.D. Stucky, Journal of the American Chemical Society 124 (2002) 13642–13643.
[42] M. Niederberger, G. Garnweitner, Chemistry – A European Journal 12 (2006) 7282–7302.
[43] G. Garnweitner, M. Niederberger, Journal of Materials Chemistry 18 (2008) 1171–1182.
[44] Y.C. Hsu, H.C. Lin, C.W. Lue, Y.T. Liao, C.M. Yang, Applied Catalysis B 89 (2009) 309–314.
[45] Y.C. Hsu, H.C. Lin, C.H. Chen, Y.T. Liao, C.M. Yang, Journal of Solid State Chemistry 183 (2010) 1917–1924.
[46] C.-H. Chen, C.-H. Liu, Y.-C. Su, C.-M. Yang, Applied Catalysis B 123/124 (2012) 36–42.
[47] H. Kato, K. Asakura, A. Kudo, Journal of the American Chemical Society 125 (2003) 3082–3089.
[48] A. Gulino, I. Fragala, Inorganica Chimica Acta 358 (2005) 4466–4472.
[49] K.J. Chao, S.P. Sheu, H.S. Sheu, Journal of the Chemical Society, Faraday Transactions 88 (1992) 2949–2954.
[50] E. Giamello, Z. Sojka, M. Che, A. Zecchina, Journal of Physical Chemistry 90 (1986) 6084–6091.
[51] P. Dutta, M.S. Seehra, S. Thota, J. Kumar, Journal of Physics: Condensed Matter 20 (2008) 152181–0152188.
[52] F. Morales, D. Grandjean, A. Mens, F.M.F. de Groot, B.M. Weckhuysen, Journal of Physical Chemistry B 110 (2006) 8626–8639.
[53] H. Zhang, Z. Ji, T. Xia, H. Meng, C. Low-Kam, R. Liu, S. Pokhrel, S. Lin, X. Wang, Y.P. Liao, M. Wang, L. Li, R. Rallo, R. Damoiseaux, D. Telesca, L. Madler, Y. Cohen, J.I. Zink, A.E. Nel, ACS Nano 6 (2012) 4349–4368.
[54] M.W. Kanan, D.G. Nocera, Science 321 (2008) 1072–1075.
[55] D.G. Nocera, Accounts of Chemical Research 45 (2012) 767–776.